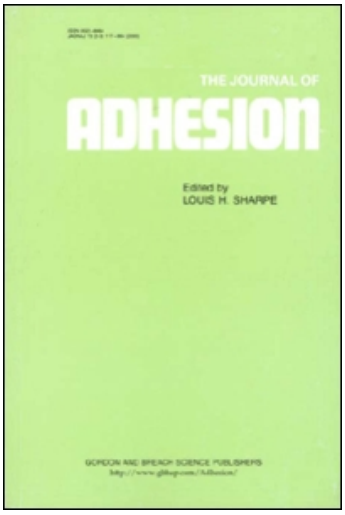

The Journal of Adhesion
Publication details, including instructions for authors and subscription information:
http://www.informaworld.com/smpp/title~content=t713453635

Fatigue fracture of fully saturated bonded joints

Kenneth M. Liechti[a]; G. Alexis Arzoumanidis[a]; Soo-Jae Park[a]
[a] Research Center, Mechanics of Solids, Structures and Materials, University of Texas, Austin, Texas, USA

Online publication date: 08 September 2010

To cite this Article Liechti, Kenneth M. , Arzoumanidis, G. Alexis and Park, Soo-Jae(2002) 'Fatigue fracture of fully saturated bonded joints', The Journal of Adhesion, 78: 5, 383 — 411
To link to this Article: DOI: 10.1080/00218460212517
URL: http://dx.doi.org/10.1080/00218460212517

The Journal of Adhesion, 78: 383–411, 2002

0021-8464/02 $12.00 +.00
DOI: 10.1080/00218460290010250

FATIGUE FRACTURE OF FULLY SATURATED BONDED JOINTS

Kenneth M. Liechti
G. Alexis Arzoumanidis
Soo-Jae Park
Research Center, Mechanics of Solids, Structures and Materials, University of Texas at Austin, Austin, Texas, USA

The objective of this study was to compare the fatigue crack growth characteristics of adhesively bonded joints at several temperatures in air and salt water. Motivated by current trends in automotive structures, the specimens consisted of urethane adhesive bonding composite adherends with swirled glass fibers in an isocyanurate matrix. A modified cracked lap shear configuration under four-point bending was used to load the specimens, which were reinforced in order to ensure that cracking at or near the interface could be examined under all conditions. Potentially ambiguous diffusion transients were removed by fully saturating the specimens that were to be tested in salt water.

Paris Law parameters and threshold values of energy release rate were extracted for each environmental condition that was studied. In air, both high and low temperatures increased crack growth rates and reduced threshold values relative to room temperature. Increasing temperature from 10°C consistently lowered the bond durability in salt water. The effects of load level, temperature, and environment on the fracture parameters were related to fracture mechanisms via recorded side views and fractographic evidence.

Keywords: Fatigue crack growth; Adhesively bonded joints; Saltwater exposure; Thermal effects

Received 24 September 2001; in final form 4 January 2002.

The authors would like to thank Mr. David Warren and Dr. Ray Boeman at Oak Ridge National Laboratories for monitoring this research, which was funded through the Lightweight Vehicles Program. In addition, a significant amount of work went into providing specimens. Thanks are also due to Dr. Kenneth Morman and Dr. Jessica Schroeder with the Automotive Composites Consortium for many technical discussions and for providing industrial relevance to the work.

Address correspondence to Kenneth M. Liechti, University of Texas, ASE/EM Department, 24th & Speedway, WRW 110, Austin, TX 78712, USA. E-mail: kml@mail.utexas.edu

INTRODUCTION

Low-cost, glass-fiber-reinforced polymer composites are being seriously considered for lightweight structural components for automobiles. Adhesively bonded joints are an attractive joining solution for such structures due to weight savings, reductions in stress concentrations, and manufacturing economies. One issue that needs to be addressed is the durability of the bonded joints in situations where the loads are repeated and the joints are subjected to harsh environments. Bearing in mind that adhesives are relatively brittle and that cracks may grow from preexisting flaws or bimaterial corners, the durability issue will be addressed via fracture mechanics in this study.

The fracture toughness of the adherend/adhesive system considered here has already been determined by Swadener et al. [1]. The adherends considered were a random swirl glass fiber in an isocyanurate matrix with two adhesives, epoxy and urethane. The bond between the epoxy and the adhesive was tough enough to cause cracks to parallel the interface in the composite. In that case, the toughness was independent of the fracture mode-mix (combination of tension and shear at the crack tip). When the urethane was employed as the adhesive, crack growth was more closely interfacial, but nonlinear viscoelastic effects gave rise to a crack tip shielding effect for mode-mix angles greater than 45°. Only the urethane was considered in this study due to severe branching into the adherends under cyclic loading in dry and saltwater environments when the epoxy was used as the adhesive.

The fracture mode-mix that was considered here was set at an intermediate level in order to match the values that arise in some typical automotive joints [2]. Only one value was considered because the effects of cyclic loading, temperature, and solvent were considered to be more important. In addition, since stress levels were lower, nonlinear effects would most likely be less dominant, thereby reducing any shielding effects. Nonetheless, it may be important to examine mixed-mode effects for large angles where frictional and asperity locking dominate.

While a number of specimens are capable of producing such mode-mix levels, the cracked lap shear (CLS) specimen was selected for this study. It has a long history of use in the adhesive fracture community, starting with the works of Roderick, Everett, and Crews [3], and Brussat and Chiu [4]. The former used a three-adherend version of the specimen while the latter study presented the specimen in its more common double adherend form, indicating that either moments or loads could be applied to the specimen. Mall, Johnson, and Everett further analyzed the CLS specimen in tension and used it to study

fatigue fracture of joints with composite adherends [5]. Johnson and Mall [6] subsequently used this specimen to study ply orientation influences on the fatigue fracture resistance of joints. Although failure was cohesive in the adherend for specimens with 45° or 90° plies at the interface, a 0° ply with respect to crack growth direction near the interface effectively guided the crack. Of course, the swirled glass fiber composite in the present study has more in common with 45° or 90° plies of unidirectional composites and would be expected to be more prone to crack branching and cohesive failure in the adherend. The CLS specimen was one of several that Lin and Liechti [7] considered in a study of transferability issues. Charalambides et al. [8] created a two-crack-front version of the CLS specimen for a bimaterial interface. Named the University of California, Santa Barbara (UCSB) specimen, it was further analyzed to include the effects of friction (Charalambides et al. [9]). An adhesive joint version of this specimen was developed by Conley et al. [10].

Mostovoy and Ripling [11] conducted one of the earliest studies on the effect of solvent on crack growth in adhesively bonded joints. For energy release rate levels between threshold and toughness, crack growth rates exhibited a power law dependence on the energy release rate per cycle. Cognard [12] used a wedge test to determine crack growth rates under static loading in steel epoxy joints. Many environments, including nonpolar and polar liquids, water, and tropical climate (40°C @ 90% RH) were considered. The fracture location changed from cohesive to adhesive as joints were exposed to environment. Nonpolar liquids did not change fracture resistance but shifted location. Polar liquids altered both the fracture resistance and location, with water being the most severe environment. Conley et al. [10] examined static crack growth in glass/epoxy/glass joints. Several different epoxies were used in a four-point bend specimen in 15% and 80% RH. Toughness values decreased at 80% RH. Subcritical growth had power law exponents in the range $2 < n < 4$, and threshold values were less than 20% of toughness values. The data from this study were later amended (Ritter et al. [13]) to account for different crack growth locations. The exponents dropped below 2. Ritter et al. [14] then added the effect of cyclic loading, which accelerated crack growth. Ritter et al. [15] looked at the effect of silane treatments on glass and fused silica on mode I toughness, static crack growth, and fatigue threshold values. Silane produced a significant improvement.

Working with more structural joints, Wylde and Spelt [16] used a special mixed-mode loading jig [17] to study moisture effects by taking advantage of an "open-faced" specimen. In this scheme, the adhesive layer was applied to only one adherend, allowed to saturate, then bonded

to the other adherend. The adhesive was therefore quickly and fully saturated prior to the experiment. They introduced a degradation parameter to combine the effects of temperature, humidity, and exposure time. It worked quite well with a Cybond 1126® adhesive. Fernando et al. [18] considered the mode I fatigue fracture of aluminum/epoxy bonded joints. Several surface treatments and dry (23°C, 55% RH) and wet (26°C, distilled water immersion 5 min prior to test) environments were considered. Threshold toughness values were used to compare effects of environment and surface treatment. Phosphoric acid etching followed by an application of primer provided the least reduction of threshold values. The damaging effect of a wet environment on fracture resistance parameters on metal/epoxy joints with galvanized steel and aluminum alloys was also noted by Jethwa and Kinloch [19]. Dickie et al. [20] conducted extensive postfracture analyses of the specimens and found that electrochemical activity was the main cause of degradation in the joints with steel adherends. Sancaktar [21] considered mixed-mode fatigue fracture in the presence of solvent using the independently loaded mixed-mode specimen.

In this study, we wished to avoid the transients that can occur when crack growth rates are similar to or outstrip diffusion rates. The out-of-plane dimension of the specimens was minimized so that they could be fully saturated prior to testing.

EXPERIMENTS

Several aspects of the experimental portion of this study required development. It was first necessary to develop a suitably reinforced specimen to produce cracks near the interface. The reinforcement led, in turn, to a specimen so stiff that a high-resolution displacement transducer had to be developed for compliance measurements. Contact between the loading device and the specimen, suitable control of the environments, and image analysis also required some attention.

Specimen

A cracked lap shear (CLS) specimen under uniform bending was selected for the experiments. Based on the work of Brussat and Chiu [4], it held the promise of energy release rates that were largely independent of crack length. Experiments were conducted on specimens that consisted of swirled glass fiber/isocyanurate matrix composite adherends (DOW MM 364®) bonded with a urethane (Ashland) adhesive. The 2.5 mm thick specimens were sliced from laminated blocks that were 178 mm square and 27.2 mm high, with the latter

dimension including a 0.8 mm layer of urethane. The relatively small specimen thickness was required in order to minimize the time for complete saturation of the specimen prior to testing. The composite adherends had a relatively low fatigue limit, which meant that crack branching was a serious problem to be overcome if the bondline itself was to be the focus of the study. The specimen was reinforced with stainless steel bars that were glued and bolted to the top and bottom of the specimen (Figure 1). This reinforcement reduced the axial stresses in the composite adherend for a given level of applied energy release rate. It also ensured that no buckling of the adherends occurred. Hysol 9296® epoxy and Place SloZAP® cyanoacrylate formed the bond for the experiments conducted in air and saltwater. The resulting reinforced specimen had an I-beam cross-section, which is illustrated in its

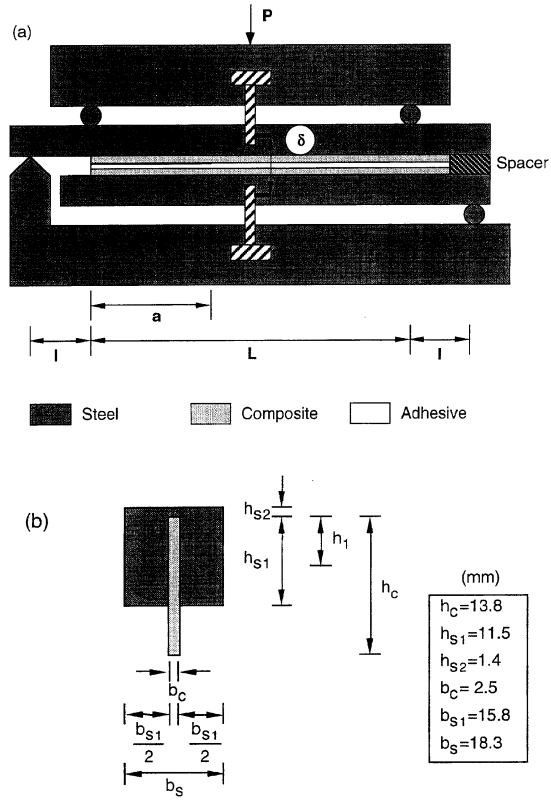

FIGURE 1 (a) Schematic of loading jig and specimen and (b) cross-sectional dimensions of a symmetric half of the specimen.

mounted position in the testing jig. The cross sectional dimensions of the specimen are shown in Figure 1b. The longer adherend was 178 mm long and the longer steel bar was 203 mm long. This accommodated a 25 mm square stainless steel spacer at the uncracked end of the specimen that effectively increased its length, thereby leading to more uniform energy release rates, as will be seen later. The span between the inner loading points was $L = 152$ mm. The distance, l, between an inner and outer load point was usually 12.7 mm. When relatively small loads were required it was decreased to 6.4 mm.

Loading and Compliance Measurements

The four-point bending load was introduced to the specimen as shown in Figure 1. The triangular contact fixed the specimen from translation in the horizontal and vertical directions while the ground steel rods introduced and reacted loads in a manner that minimized friction.

Crack length was primarily monitored via compliance measurements, with compliance being defined as

$$C = \frac{\delta}{P}. \tag{1}$$

It was necessary to measure load and displacement. A 22.2 kN Sensotec load cell was used to measure the load, P. The relative displacement, δ, of the loading bars was measured with two high-resolution differentially variable reluctance transducers (DVRT). This device has a resolution of 60 nm, which means that it needs to be mounted in a permanent fixture that then makes the connection with the specimen. The fixture that was used here relied on parallel flexure elements (Figure 2) to support the transducers and mount to cylindrical rods that were attached to the upper and lower loading bars. The flexures transformed the ultrasensitive DVRT into a robust and easily mountable extensometer. The knife edge contacts of the extensometer were attached to the cylindrical rods and accommodated the rotation caused by some horizontal displacement of the rods due to the asymmetry of the specimen.

A custom LabVIEW driver commanded an Instron model 8500 digital servohydraulic controller over a general purpose interface bus and acquired data with a 16 bit A/D board. Digitally filtered raw data files of load and average displacement were taken over two cycles at selected intervals. Experiments were conducted in load control at 11 Hz with a minimum/maximum load ratio of $R = 0.1$. Cracks were

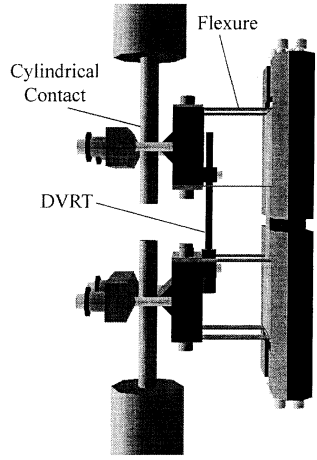

FIGURE 2 Displacement transducer attached to the mounts on the loading jig.

initiated in the adhesive layer with a razor blade. Fatigue cracks were grown in approximately 6 mm increments so that data for 6 to 8 maximum energy release rate levels could be obtained from each specimen. Generally, lower load levels were applied before higher ones, since the larger fracture process zone due to higher energy release rate levels could retard cracks that were subsequently grown at lower levels. The exception to this was for the lowest energy release rate levels, where the razor starter crack was not sharp enough to initiate growth. Here, a fatigue crack grown at a higher energy release rate served as the starter crack.

To conduct experiments above or below room temperature, the entire load train, including displacement transducers, was placed inside a BEMCO environmental chamber. To measure temperature, a thermocouple was placed in direct contact with the specimen. Experiments conducted in saltwater were accomplished by building a solvent tank whose floor was the top surface of the bottom bar of the loading jig. Full saturation of the specimens was ensured by a two-year saltwater soak.

Six environmental cases were considered: 10, 26, and 90°C in air and saltwater. The high temperature, saltwater environment proved to be the most challenging one. Some modifications were required. Specimens were considerably less stiff than the other five cases, so the moment arm (l in Figure 1) was reduced from 12.7 mm to 6.35 mm. This placed the compliance measurements into a more reasonable

range for the transducers. In addition, there was a problem with evaporation, which was solved by installing a freshwater reservoir. The reservoir was gravity fed and manually adjustable so that it could drip water into the solvent tank, replenishing evaporation losses. Finally, the solvent occasionally splashed up onto the top surface of the specimen, leaving behind salt crystals which inhibited rolling at the contact points. Oiling the contact points before the experiment alleviated this.

ANALYSIS

The specimen and loading shown in Figure 1 correspond to a CLS specimen under uniform bending. If we ignore the presence of the 0.8 mm urethane adhesive layer, the energy release rate for a crack in the uniform bending segment is given by

$$G_{\text{beam}} = \frac{M}{2E_s b_c}\left[\frac{1}{I_L} - \frac{1}{I_R}\right]. \tag{2}$$

M is the uniform bending moment between the two inner load points, and E_S is the Young's modulus of the steel. The quantities I_I and I_R are, respectively, the moments of inertia of the composite beams behind and in front of the crack tip. They are given (with reference to Figure 1b) by:

$$I_L = \frac{1}{12}\left[b_{s1}h_{s1}^3 + b_s h_s^3 + b' h_c^3\right] + b_{s1}h_{s1}\left[h_1 - \frac{h_{s1}}{2}\right]^2 + b_s h_s\left[h_1 + \frac{h_{s2}}{2}\right]^2 + b' h_c\left[\frac{h_c}{2} - h_1\right]^2 \tag{3a}$$

and

$$I_R = \frac{b_{s1}h_{s1}^3}{6} + 2b_{s1}h_{s1}\left[h_c - \frac{h_{s1}}{2}\right]^2 + \frac{b_s h_s^3}{6} + 2b_s h_s\left[h_c + \frac{h_{s2}}{2}\right]^2 + \frac{2}{3}b' h_c^3, \tag{3b}$$

where

$$h_1 = \frac{b_{s1}\frac{h_{s1}^2}{2} + b'\frac{h_c^2}{2} - b_s\frac{h_{s2}^2}{2}}{b_{s1}h_{s1} + b'h_c + b_s h_{s2}}, \quad b' = nb_c,$$

and

$$n = \frac{E_c}{E_s}.$$

The quantity E_c is the Young's modulus of the composite.

The analysis indicates that the energy release rate should be independent of crack length for a long enough specimen. However, the length-to-height ratio of the specimen in the constant moment section was about 5, which is not large enough for a beam theory analysis to be valid. As a result, a linear elastic, small, and plane-strain finite element analysis (FEA) was developed to determine the energy release rate and mode-mix as a function of crack length.

The finite element model consisted of 1600 degrees of freedom. A refined mesh around the crack tip was shifted in 12.7 mm increments to simulate different crack lengths. Boundary conditions were applied to four nodes in the model as shown in Figure 3. To account for friction at the rolling pin contact points, point loads, F, were applied opposite to the direction of rolling. The coefficient of friction, μ, was therefore

$$\mu = \frac{2F}{P}. \tag{4}$$

As will be seen shortly, the value of the coefficient of friction was selected in such a way that solutions for the specimen compliance matched the measured values from a specimen in a dry environment at room temperature. Once friction issues were resolved, each combination of temperature and environment that was used in the experiments was modeled individually using the average dimensions of the specimens that were actually tested and the material properties (Table 1) unique to each case. This exercise resulted in 6 separate curves of normalized compliance and energy release rate versus crack length. These curves were later used in data processing. The local mode-mix was obtained directly via a postprocessing module in ABAQUS.

Compliance Analysis

The calibration experiment was conducted at room temperature in a dry environment. A specimen was placed in the loading jig and a load cycle was applied at subcritical energy release levels to several

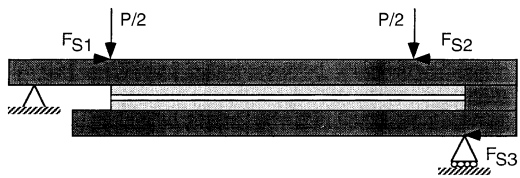

FIGURE 3 Boundary conditions for the finite element analysis.

TABLE 1 Elastic Properties for the 6 Environmental Conditions

Case	Adhesive Poisson's ratio, ν_a	Adhesive modulus $E_a(GPa)(psi)$	Composite Poisson's ratio, ν_c	Composite modulus $E_c(GPa)(psi)$
10°C, air	0.390	1.5 (2.20×10^5)	0.293	9.65 (1.40×10^6)
26°C, air	0.403	0.88 (1.28×10^5)	0.294	9.30 (1.35×10^6)
90°C, air	0.499	0.09 (1.43×10^4)	0.297	7.65 (1.11×10^6)
10°C, SW	0.390	0.61 (8.80×10^4)	0.2933	8.68 (1.26×10^6)
26°C, SW	0.403	0.35 (5.12×10^4)	0.294	8.41 (1.22×10^6)
90°C, SW	0.499	0.04 (5.72×10^3)	0.297	6.88 (9.99×10^5)

SW, salt water.

different cracks. A hack saw blade of the same thickness as the bondline was used to remove the adhesive to known lengths. These artificially grown cracks were monitored optically with a Questar® telescope and a 0.254 mm resolution rule on the specimen. Compliance was determined from the load-displacement response of two consecutive cycles. This compliance measurement was repeated 10 times at each crack length and averaged.

Designing the contact points of the 4-point bending jig was not straightforward, and several combinations of contact point geometries were considered. The final iteration had a triangular geometry for one of the bottom contact points, as in the outer left contact point in Figure 1. This fixed the specimen horizontally in space, preventing any rigid body translation that would complicate crack length determination. The other 3 loading points were rolling pins cut from 12.7 mm diameter, ground stainless steel shaft stock, which minimized friction effects on compliance.

The results from the experiments and finite element analyses are compared in Figure 4. The ordinate represents the change in compliance from an arbitrary reference. Data are plotted in this manner because the computational model did not account for 2 factors that contributed to the values of compliance that were measured: contact point effects and displacements in the jig that occurred between the extensometer mounts. The reference compliance was taken at $a/L = 0$. In addition, the energy release rate is proportional to the rate of change of compliance with crack length $\frac{\partial C}{\partial a}$.

The predicted value of $\frac{\partial C}{\partial a}$ from the finite element analysis with zero friction was about 8% higher than the corresponding measurements. When rolling friction was included in the rolling pin contacts with a coefficient of friction $\mu = 0.054$, the $\frac{\partial C}{\partial a}$ values from the analysis and the

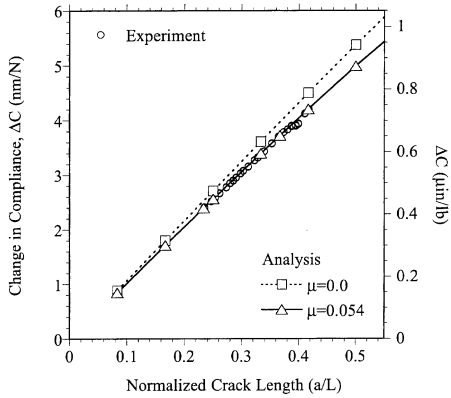

FIGURE 4 Compliance change relative to initial measurement plotted against crack length normalized by the distance between the central loading points.

experiment were brought into agreement. This value of friction coefficient, which is reasonable for steel rolling on steel, was used in all subsequent analyses.

Since the finite element model agreed with the saw cut experiments at room temperature in a dry environment, each of the 6 permutations of 3 temperatures and 2 environments were numerically simulated using their particular average dimensions and material properties. The composite and urethane adhesive tensile moduli in air that are listed in the Table 1 were measured at the 3 temperatures. The softening effects of salt water on the adhesive and composite were obtained by scaling the corresponding dry cases by 0.4 and 0.9, respectively. This was based on estimates of the effect of the salt water [2].

The first set of results from these simulations is shown in Figure 5, where compliance normalized by the compliance at $a = 0.9L$ is plotted against normalized crack length. The plot shows that, for all of the cases, compliance was almost linearly related to crack length for about 65% of the gage length between the central loading points. It also shows that, except for the 90°C case, the slopes of the linear sections were essentially equal, which is a direct result of the stiffening from the steel bars common to all cases. The key difference between these simulated cases was the stiffness of the adhesive. The adhesive material properties had a startling effect on the fracture properties, considering the common practice of ignoring their effect on the overall system. This is probably due to the relatively thick bondline that was used here.

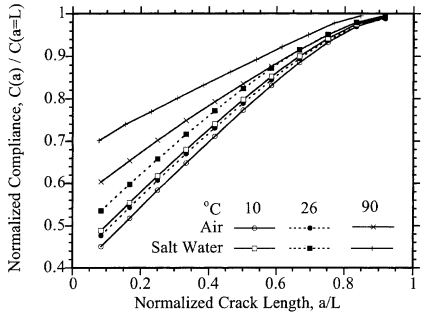

FIGURE 5 Simulated variation of normalized compliance with normalized crack length for the various environmental conditions considered.

Energy Release Rate Analysis

The variation of J-integral with crack length and environmental condition was then extracted from the finite element analyses. Since these were all linear elastic analyses, J-integral values were equivalent to the energy release rates. The J-integral values were normalized by G_{beam}, the beam theory prediction for energy release rate without contact point friction. Figure 6 portrays 8 cases of normalized J-integral versus normalized crack length. This included the 6 conditions under which the experiments were conducted and 2 frictionless cases. The latter utilized the same material properties and dimensions as the room temperature air model, but one of them retained the steel spacer while the other did not.

The result for the spacer and no friction followed the beam theory prediction to within $\pm 2\%$ for the first half of the gage length, after

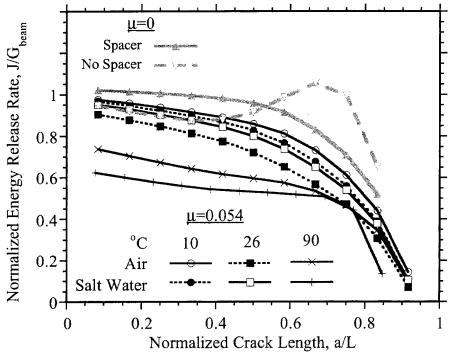

FIGURE 6 Normalized energy release rate calibration with crack length for the various environmental conditions considered.

which point the energy release rate associated with the specimen deviated more and more from beam theory. The forces applied to the bonded portion (right side) of the CLS specimen were the likely cause of this deviation. The stainless steel spacer apparently shielded the crack tip from some of the effects of the force couple. This claim is strengthened by the second frictionless result where the energy release rate in the absence of the spacer gave rise to fluctuations (Figure 6) in energy release rate for very long cracks.

For sufficiently long CLS specimens under 4-point bending, the energy release rate is independent of crack length. This was essentially the case with the actual specimen dimensions and no friction, at least for the first half of the gage section. However, including friction at the contact points caused a much sharper decrease in energy release rate with crack length, particularly in the second half of the gage length. As a result, all data reported in this study were obtained for $a/L < 0.5$.

The simulations of the 6 different environments gave rise to a surprising influence of the composite and adhesive material properties on the values of energy release rate, considering the much larger stiffness of the steel reinforcements and the common assumption that the adhesive layer has small influence. Suo and Hutchinson [22] used the path independence of the J-integral to argue that energy release rate values based on adherends alone (global) and local values (including the adhesive) were the same. This meant that the energy release rate could be determined from the deformations of the stiffer adherends. The differences seen here are most likely due to the more complex stress state that occurs with the combination of steel reinforcement, composite adherends, and an adhesive layer. The results emphasize that all components must be modeled in such reinforced specimens, particularly considering the unreinforced height of the composite. In addition, it should be noted that the adhesive layer was much thicker than usual and could not, therefore, be ignored.

Mode-Mix

Fracture criteria for structural joints often involve not only the magnitude of energy release rate but also mode-mix. The range of mode-mix that the CLS specimen used in this study provides over the span of conditions that were considered was determined as part of the finite element analyses that was conducted. The standard postprocessing option in ABAQUS was used for this purpose.

For $a < L/2$, it can be seen (Figure 7) that the local mode-mix ranged from -18° to 10° for the 10 and 26°C environments and from -44° to

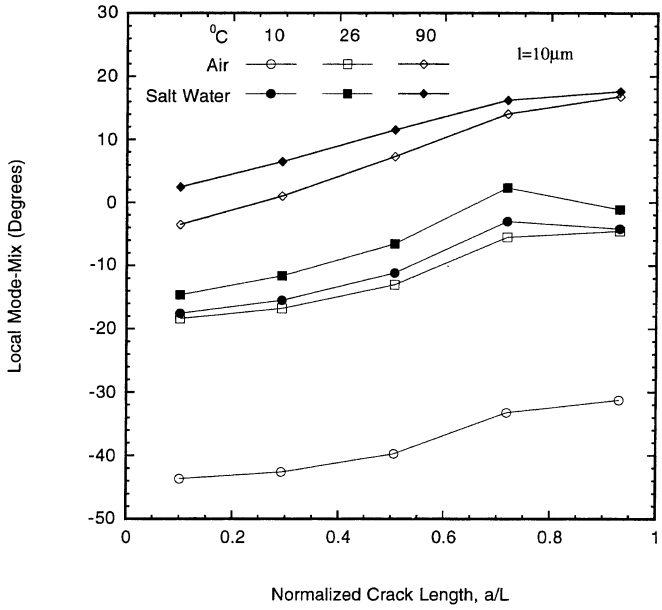

FIGURE 7 Calibration of local mode-mix with crack length for the environmental conditions considered.

10° for all environments. Even over this broader range, Swadener et al. [1] found that the toughness of these urethane joints was independent of mode-mix. Thus, mode-mix effects were not expected to be apparent for the range of crack lengths considered in the experiments that were conducted in this study.

DATA REDUCTION

The basic experimental data and finite element results were combined in the data reduction procedure. The experiment produced files of maximum load, change in compliance, and cycle number, N, at a given load level. These data were processed using the relationships from the finite element solutions to produce the correlation between crack growth rates and maximum energy release rates in a cycle.

Crack Length

Crack length was determined through compliance measurements. Nonlinear effects introduced by the contacts between loading jig and

specimen complicated the analysis of compliance data. One way of avoiding the contact point nonlinearities is to define the compliance as the slope of response beyond a high enough load level that contact point effects are insignificant. However, an alternative method offered higher precision.

To circumvent nonlinear effects, the change in compliance, ΔC, relative to compliance at the first cycle of a given load level was monitored during the experiment. To find ΔC, consider first that the compliance of the system is the sum total of compliance of each element. The initial cycle at a given load level has both the linear contribution from the specimen and the nonlinear contribution from the contact points. Neither of these values is critical for data analysis in this fatigue fracture experiment, as the key data concerns the change in compliance with crack length. Therefore, if the compliance of the first cycle could be subtracted from the compliance values of all subsequent cycles, both the linear contribution from that first cycle and the nonlinear contact point contribution constant in all cycles is removed, leaving behind only the crucial data of compliance change.

The first step in determining ΔC was to measure displacement and load during the initial cycle. From these discrete data, a continuous function for displacement as a function of load could be created for the first cycle. This function was named $\delta_0(P)$ and took the form of a quadratic interpolation of discrete data. The change in compliance was therefore defined by

$$\Delta C \equiv \frac{\delta(P) - \delta_0(P)}{P}, \tag{5}$$

where $\delta(P)$ was the response on subsequent cycles. Each recorded entry for ΔC was found from the slope of a linear regression analysis performed on $(\delta(P) - \delta_0(P))$ versus P data from 2 consecutive cycles once every 5 cycles.

Once ΔC data was established, crack length was obtained via a three-step process. First, the known initial crack length was converted to an initial compliance, C_o, based on the finite element results that were already presented in Figure 5. The first entry of ΔC was added to this in order to obtain the new compliance value, which was converted back to crack length, again using the calibration in Figure 5. The process was then repeated for each new ΔC value.

The crack length data for any given load level was run through a smoothing filter, which computed the moving average through a sliding window of size N_w. The derivative was computed from the slope of a linear regression analysis on the smoothed crack length data and

the corresponding number of cycles in an identically sized sliding window. The result was a vector of da/dN data for that $G_{\max}$ level.

The number of cycles in a window was determined from an experiment that was conducted on a dummy specimen machined from a block of stainless steel. Here, there was no crack growth, so da/dN should have been zero. Data from 40,000 cycles were analyzed with different-sized windows, and the results indicated that for 2% error window size and change in compliance with number of cycles (dC/dN) were related by

$$N_w = \frac{B}{dC/dN}. \tag{6}$$

The parameter B in this experimental setup was 2.85×10^{-8} mm/N (5×10^{-9} in/lb). As a result, the data reduction procedure first involved determining an approximate value of dC/dN for a given point, then calculating the appropriate window size, and finally running the smoothing filter and taking the derivative with the appropriate window size. Each point plotted in the resulting fatigue fracture resistance curves was based on 0.127 mm (0.005 in) of growth.

Combining data for crack length and the applied maximum load, P_{FE}, with the finite element results in Figure 6 meant that the maximum energy release rate, $G_{\max}$, in any particular cycle could be determined by the scaling

$$G_{\max} = G_{FE}\left(\frac{P_{\max}}{P_{FE}}\right)^2, \tag{7}$$

where P_{FE} refers to the load level that was used in the finite element analysis and G_{FE} was the corresponding energy release rate value.

FATIGUE CRACK GROWTH RESISTANCE

The fatigue fracture experiments were conducted at 3 temperatures in environments of air and salt water. Figure 8 depicts the 6 curves that represent the resistance of the urethane/composite interface to fatigue crack growth. Typical scatter is indicated in the 26°C, air case. Though reasonable, scatter was noticeably higher for the 90°C cases. The arrow near the start of each set of data indicates the threshold value of energy release rate, G_{th}.

In each case, the data were fit to the Paris Law defined here as

$$\frac{da}{dN} = A(G_{\max})^n. \tag{8}$$

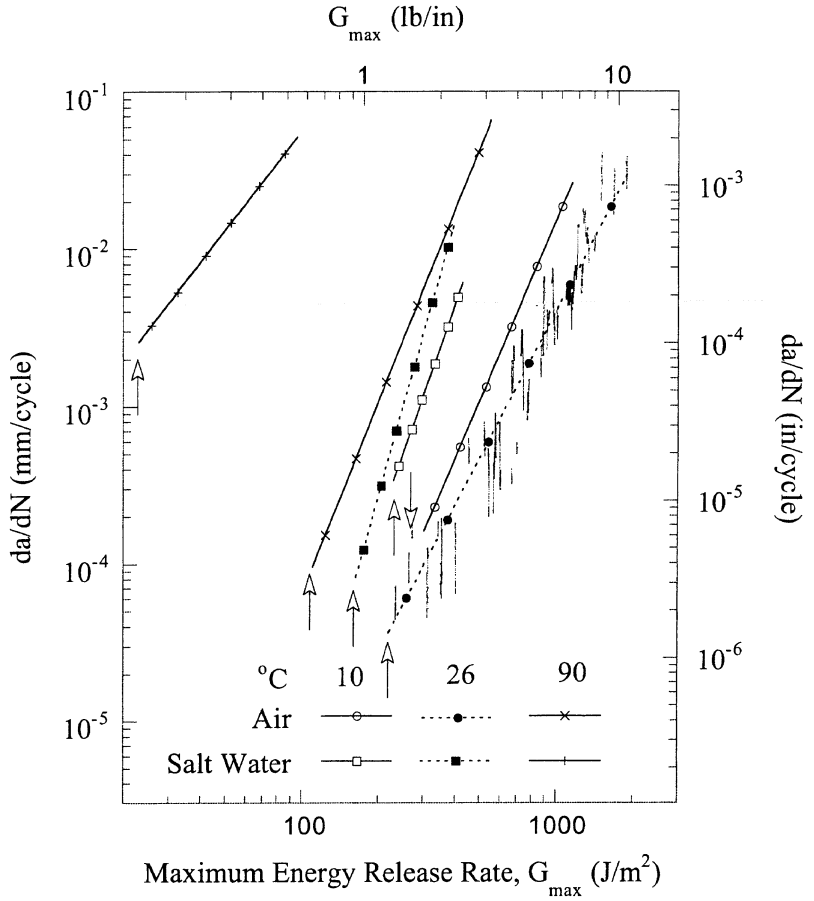

FIGURE 8 Resistance to fatigue crack growth for the various environmental conditions considered. The arrows represent the threshold values of energy release rate.

The parameters A, n, and G_{th} for each environmental condition are listed in Table 2. The values of n ranged from 2.10 to 5.82, which are generally lower than the values obtained by Dessureault and Spelt [23], Fernando et al. [18], and Jethwa and Kinloch [19] for the various structural bonded joints that they considered. Ritter et al. [13] quoted values of 1.6 to 1.8 in their work with glass and various epoxies. In this study, with the air environment at 26°C as a reference, both higher and lower temperatures in air gave rise to higher exponents n. Over the range of $G_{\max}$ values that were considered, the higher and lower

TABLE 2 Paris Law Parameters for Joints Under Various Environmental Conditions

Temperature (°C)	Environment	$A\left(\frac{m}{cycle}\left(\frac{m^2}{J}\right)^n\right)$	Exponent n	Threshold $G_{th}(J/m^2)$
10	Air	5.60×10^{-17}	3.81	269
26	Air	1.88×10^{-15}	3.11	219
90	Air	5.06×10^{-16}	4.05	108
10	SW	3.26×10^{-18}	4.66	232
26	SW	1.80×10^{-20}	5.82	159
90	SW	3.52×10^{-9}	2.1	22.8

SW, salt water.

temperatures in air both gave rise to higher crack growth rates at a given $G_{\max}$ level than the air environment at 26°C. In salt water, both increasing and decreasing temperature relative to the room temperature reference reduced the power law exponent. With the reference temperature at 10°C we see that increasing the temperature increased crack growth rates over the range of $G_{\max}$ values that was covered in saltwater.

With the exception of the hottest saltwater environment, the exponents were fairly high ($3.11 \leq n \leq 5.82$), which means that small changes in $G_{\max}$ level lead to large variations in crack growth rates. As a result, it has become common to use threshold levels of energy release rates as measures of resistance to environmentally assisted crack growth. The G_{th} values found here (Table 2) were somewhat lower than those found by by Wylde and Spelt [16], Fernando et al. [18], and Jethwa and Kinloch [19] for structural adhesives. In air, $108 \leq G_{th} \leq 269$ J/m^2, and raising and lowering the temperature from 26°C reduced the threshold levels, more so at 90°C than at 10°C. When the specimens were exposed to saltwater, $22.8 \leq G_{th} \leq 232$ J/m^2, and raising the temperature from 10°C resulted in a decrease in threshold values, particularly at 90°C.

CRACK GROWTH OBSERVATIONS

Several observations of crack growth were made both during and post-fracture. The former was made via optical microscopic observations of one of the sides of the specimen that was intersected by the crack. Image processing was used to enhance the views of the crack tip and fracture process zone. Post fracture analyses were made with a scanning electron microscope. Both helped shed light on fracture mechanisms.

Side Viewing of Cracks

The first step in the optical crack measurement technique involved obtaining a digital image of the side of the specimen for the open and closed crack in a given cycle without changing the loading frequency during image capture. To this end, a 1024×1024 resolution, 256-level grayscale, high-speed Kodak digital camera was mounted to a Wild Macroscop 450, low-magnification microscope. The camera was rotated at 45° to the horizontal in order to maximize the number of pixels along the crack path. To obtain an image at the extrema of a load cycle, the capture rate was set to 15 Hz. This frequency was out of phase with the 11 Hz of the loading sinusoid such that in one second, images were taken every 24°. Even though they were not captured from the same cycle, images captured over one second were used to approximate images from a single cycle at 24° increments. The 24° increment meant that one of the 15 images was at most 12° away from the maximum and minimum of this constructed cycle, which led to a 2% difference between extremum and image. Since the image resolution was coarser than this 2% difference, 15 images were deemed sufficient to capture frames of the maximum and minimum effectively. Only the opened and closed crack images were saved for postprocessing.

Examples of images of open and closed cracks are shown in Figures 9a and 9b, respectively. In postprocessing, the open image was subtracted from the closed image in an attempt to highlight the crack. Before subtracting, the open image had to be shifted relative the closed one in order to account for displacements caused by the 4-point bending cycle. This shifting can be based on either the top or the bottom of the specimen. Figure 9c depicts the subtraction results from a shift based on the bottom of the specimen. Since zero is black and 255 is white, a simple subtraction would have yielded a dark result, so 128 was added to the value of each pixel in this image, making the features on the bottom of Figure 9c a flat gray valued at about 128. The fourth image of the figure is a typical result when the shift is based on the top of the specimen. Notice that the top of Figure 9d is flat gray. Finally, the subtracted images were multiplied together in order to highlight the crack morphology. The result is a Gaussian distribution centered around 60 and ranging to ± 35 grayscale levels. To facilitate viewing, the bell curve was spread over the 256-level grayscale range, an example of which is shown in the final row of the figure. The perceived crack tip location and fracture process zone are indicated in Figure 9e.

The processed digital images were compared with crack length measurements based on compliance. Examples of such comparisons

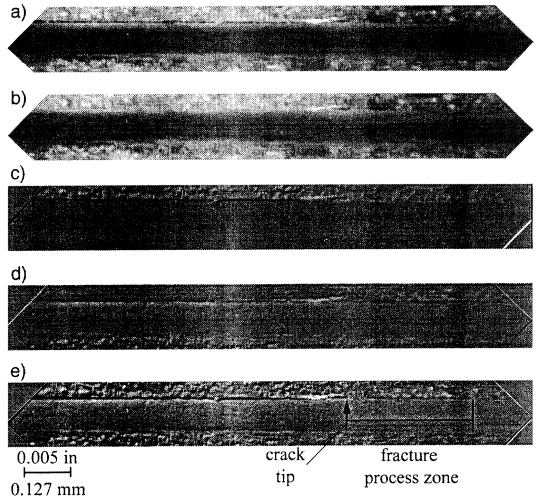

FIGURE 9 Steps in the digital image processing process: (a) open crack, (b) closed crack, (c) open minus closed, shift based on bottom, (d) open minus closed, shift based on top, (e) multiplied image, highlighting the crack.

for an experiment conducted in air at 26°C and $G_{max} = 683$ J/m^2 (3.9 lb/in) are shown in Figure 10. Here, arrows representing crack length according to compliance are placed above a corresponding processed digital image. This arrow trails, leads, or matches the position of the crack tip determined optically, as indicated by the vertical arrow in the 4 images. An explanation for this is that the crack does not consistently grow along a straight front. It may be leading from the sides inward or from the interior of the specimen outwards. In addition, as the crack grew, the fracture process zone became larger and more complex. The growing process zone and the nonuniform front bring into question any crack measurement technique that relies on the side surface of the specimen.

Both in situ optical monitoring and the analysis of images of failed specimens provided a record of the crack path in the mixed-mode fatigue experiments conducted on this swirled glass fiber composite adherend/urethane adhesive system. Various crack paths are sketched in Figure 11. As expected from the sign of the shear being applied in this experiment, by far the most prevalent crack path was along the upper interface (Figure 11a). However, there were times when the crack also grew along the lower interface (Figure 11b). For high G_{max} levels, crack path selection was more complex as cohesive failure combined with interfacial growth.

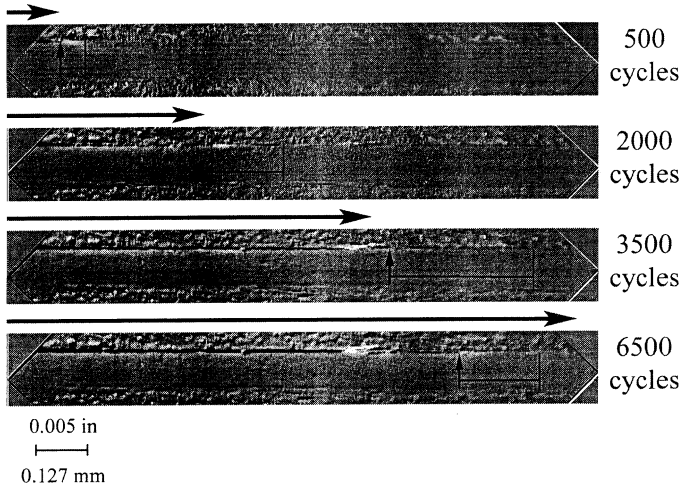

FIGURE 10 Crack length determined by compliance (horizontal arrows) compared with subtracted images of specimen side surface. Crack tip and fracture process zone indicated.

An interesting crack growth mechanism in the fracture process zone was crack jumping, as shown in Figures 11c–11e. Here an interfacial crack jumped to either the other interface, the composite adherend, or the adhesive for 1–4 bond lengths, then continued on in the original path. As the crack continued to grow, the 2 cracks in the original interface connected, concealing the event from postfailure observation.

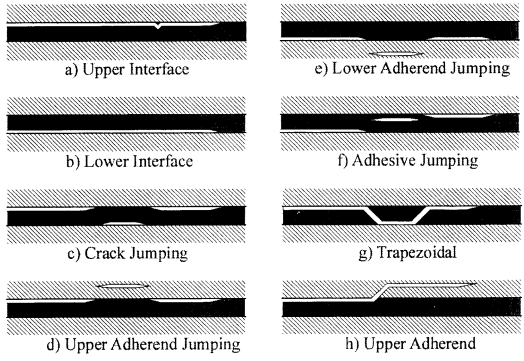

FIGURE 11 Various crack path morphologies observed from the side of the specimen.

Cracks followed the interface for all but the highest half-decade of growth rates, when the applied G_{max} level approached the critical value G_c. The macroscopic adhesive failure took 2 forms. First, there was adhesive crack jumping, as shown in Figure 11f. Here, the crack did not necessarily return to the interface where it started. Second, the crack would grow in a trapezoidal fashion, as Figure 11g shows. The top or bottom of this trapezoid was 1–4 bond thicknesses long and was not necessarily one of the two bimaterial interfaces. Such trapezoidal behavior has been seen in static fracture experiments on an aluminum/epoxy system by Chai [24], but it was periodic and attributed to residual stresses. Here, the mechanism is not periodic and, therefore, not likely the result of residual stresses.

For the saltwater water cases, crack paths were rougher than those from the experiments that were conducted in air. Although the crack followed the interface quite closely, it tore a considerable amount of fibers and matrix off the composite. Under saltwater low-temperature conditions, the crack occasionally grew in the upper adherend close to the border of the cyanoacrylate adhesive that was used to bond the steel bars to the specimen (Figure 11h).

Fracture Surfaces

The fracture surfaces of selected specimens were examined on scales of 1000, 100 and 10 μm (0.04, 0.004, 0.0004 *in*). To discern the effects of energy release rate on the fracture surface, one mid-level G_{max} value at each of the 3 temperatures and 2 environments was considered. To determine the effects of load level, 3 G_{max} levels in the room temperature air condition were also considered. Since the mid-level G_{max} value in the air case was common, this led to 8 permutations altogether. An optical microscope served for the largest scale, and a scanning electron microscope was used to explore the other two smaller scales.

1 mm Scale

The optical microscope revealed surface features that were unique to variations in G_{max} level. The top row of Figure 12 shows low, medium, and high values of G_{max} for the air environment at room temperature. The top and bottom parts of each subfigure correspond to the top and bottom fracture surfaces of each specimen. In the low and medium G_{max} cases, the upper images show the composite surface, because the crack grew along the upper interface. In the high G_{max} case, both fracture surfaces were urethane, indicating that failure in this section was cohesive in the adhesive. The key differences in the

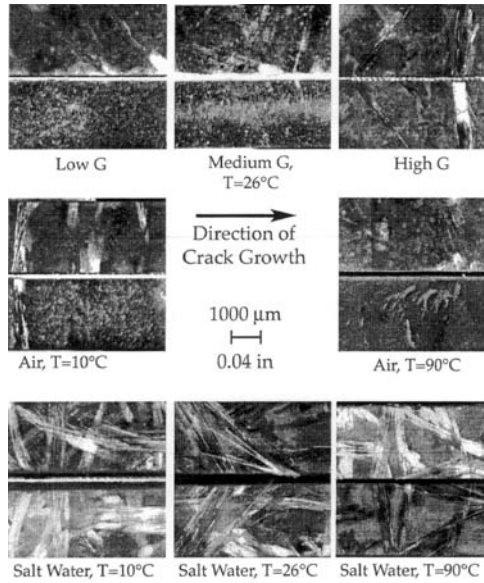

FIGURE 12 Typical optical microscope fractographs on the order of 1000 μm for the various environmental conditions.

fractographs lie in the urethane on the lower fracture surface, and attention should be focused there. At low G_{max} levels, the surface was rough and uniform across the width of the specimen. At medium G_{max} levels, the surface was smoother and there was a whitened region in the central part of the specimen. There were also some short, whitened lines perpendicular to the crack growth direction. At high G_{max} levels, the adhesive failure surface had a significant out-of-plane component and was uniform across the width. Whitened lines that extend across much of the specimen width formed flakes that were arranged on the fracture surface like shingles on a roof.

The middle row of Figure 12, together with the central image of the top row, reveals the effect of temperature for experiments that were conducted in air. All of these examples were from experiments that were conducted at medium G_{max} levels where the failure surface followed the upper interface. The upper, composite side of the interface was similar in all three cases, although there was some fiber pullout at the lowest temperature, probably due to matrix embrittlement. Features on the adhesive fracture surface at low temperature were similar to the low-level G_{max} case, though slightly coarser. The high temperature case, though apparently planar on this scale, bears

a similarity to the high G_{max} level case, with broad, white, shingled flakes across the thickness. The last row of pictures in Figure 12 reveals the source of the roughness of the interfacial failure in the saltwater experiments. The solvent weakened the composite and the crack tore off fibers. The quantity of removed fibers, and therefore the roughness, increased with decreasing temperature.

100 μm Scale

We now consider fracture surface features on a scale 1 order of magnitude smaller than the optical images just described. The top fractograph in Figure 13 depicts 3 features found at a 100 μm (0.004 in) scale. First, and common to all 3 fractographs in the figure, the rough background surface was the urethane adhesive. The whitened flakes seen on the previous scale show up as ridges, an example of which runs vertically through the middle of Figure 13a. The horizontal stripes represent matrix material that has been torn away from fiber bundles, which now lie exposed on the opposite surface. Figure 13b shows smooth exposed fibers, as well as river lines in a section of pure matrix material. The image also shows some of the rough urethane in the top right hand corner. Figure 13c is from

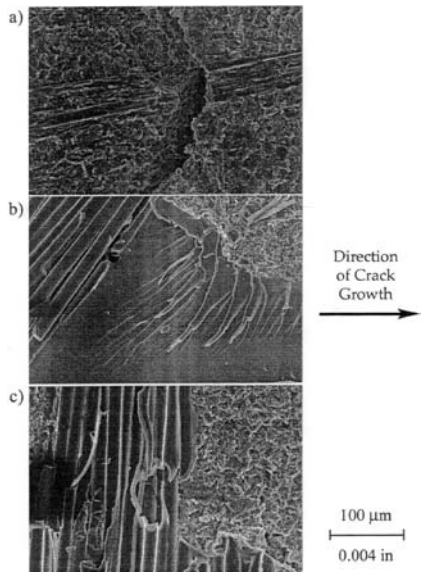

FIGURE 13 Typical features from scanning electron microscope fractographs on the order of 100 μm.

a saltwater environment experiment and shows how the solvent weakens the fiber/matrix interface. The isocyanurate matrix in the center of the image was cleanly separated from the glass fibers.

The rough urethane surface feature dominated both the top and bottom surfaces of the fracture for experiments conducted in air, implying that what appeared to be interfacial failure on the 1 mm scale was in fact cohesive in the adhesive. The fraction of surface area containing this rough feature did not depend on load level, although the size and frequency of ridges increased with increasing G_{max}. This relationship is similar to the increase in the number of whitened flakes that were seen at the larger scale. The proportion of urethane in the fractographs did decrease as temperature increased. Patches of fiber bundles, neat matrix, or stripes of matrix left behind when fibers pulled out replaced the dominant feature on portions of the surface. Still, even at the highest temperature, the adhesive accounted for about 80% of both the upper and lower surfaces for experiments conducted in air.

For saltwater experiments, there was less cohesively failed urethane on the fracture surfaces, ranging from about half to only 20% of the total surface area. The proportion decreased with increasing temperature, a trend opposite to indications from the 1 mm scale. The solvent seemed to attack the matrix/fiber interface, weakening the composite's resistance to fatigue fracture and increasing the portion of the fracture surface that was covered with fibers or matrix. An interesting point is that the crack tended to stay near the interface, even though it grew mainly in the adherend and might have been expected to branch away from the adhesive layer. The patches of failed urethane represent weaknesses in the adhesive layer that apparently kept the mixed-mode crack near the interface.

10 μm Scale

The smallest scale that was considered was on the order of 10 μm. The urethane exhibited various degrees of roughness for the 8 different cases, which can be correlated with load level and growth rate. Figure 14 contains typical fractographs on this scale, shown vertically in order of roughness. Figure 14a is an example of the smoothest case. Here, there are broad, sweeping individual tears in the adhesive. The central fractograph is similar, but the broad tears have rougher features within them, resembling the surface pattern of an autumn leaf. Most cases resembled these two. The third image is most distinct among all cases in that it contained the roughest features, where the broad, sweeping tears are replaced by high surface roughness.

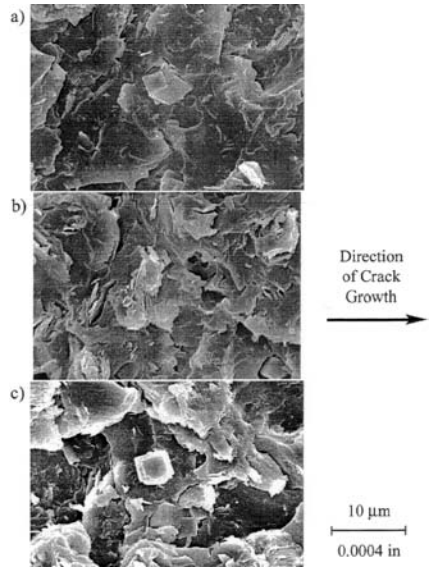

FIGURE 14 Surface roughness from scanning electron microscope fractographs on the order of 10 μm.

The images of Figure 14 are from room temperature experiments conducted in air with different G_{max} levels. Surprisingly, the order from smoothest to roughest was medium, high, and low G_{max}. The order for the effects of temperature, also in order of roughness, was room, low, then high temperature. In saltwater, the roughness order was low, room, then high temperature. So, when comparing different temperatures and keeping to the medium G_{max} level, the rougher the surface, the faster the growth rate. The sequences for varying temperature in each environment correspond well with the ordering of the growth rates in the fatigue resistance curves (Figure 8).

Two further points can be made concerning the scanning electron microscope fractographs. Firstly, there was no obvious feature across the width of the specimen in the room temperature air environment that could differentiate the whitened stripe down the mid-thickness that was seen in the optical microscope fractographs of Figure 12. Secondly, although they are over-represented in Figure 14, the fracture surface contained crystals at the interface. Although they stiffen the adhesive, these crystals are probably a source of stress concentration, which could increase crack growth rates locally.

CONCLUSIONS

The fatigue crack growth behavior of structural adhesive joints was examined over a range of temperatures in air and saltwater. The specimens consisted of swirled glass fiber/isocyanurate matrix composite adherends (DOW MM 364) bonded with a urethane (Ashland) adhesive. A specially reinforced specimen was required to ensure that buckling of the very thin specimens and excessive crack branching into the adherends did not occur. A cracked lap shear configuration under 4-point bending was used to provide mode-mix levels that are typical of bonded joints. The stiff reinforcement meant that specimen compliance had to be measured by a very sensitive displacement transducer, and contact effects at load points had to be carefully considered both experimentally and in the finite element analysis. Once finite element solutions for compliance at room temperature were reconciled with measured values, the former were used to determine energy release rate values for all the environmental conditions that were considered. These were used in conjunction with crack length measurements via compliance to determine fatigue crack growth resistance curves. The data fit well to Paris Law behavior, and fatigue thresholds were established for each condition. The power law exponents found in this study were somewhat lower (2.10 to 5.82) than those found in others. The threshold values, which ranged from $108 \leq G_{th} \leq 269$ J/m^2 in air and $22.8 \leq G_{th} \leq 232$ J/m^2 in saltwater, were somewhat lower than those quoted in previous studies. This may be due to the longer exposure to solvent. In the air environment, the lowest crack growth rates and highest threshold value were at room temperature. Lower and higher temperatures both lowered thresholds and increased crack growth rates. The saltwater led to decreases in threshold values and increases in crack growth rates with increasing temperature. Overall, saltwater at 90°C was the most severe environment in terms of the threshold values and crack growth rates. Interestingly, it produced the lowest power law exponent. Several crack growth mechanisms were observed but crack growth at the upper composite/urethane interface dominated in the air environment. Rougher surfaces and adherend involvement were more noticeable in saltwater.

REFERENCES

[1] J. G. Swadener, K. M. Liechti, & Y.-M. Liang. Shear induced toughening in bonded joints: Experiments and analysis. *Int. J. Fracture*, to appear. Also Engineering Mechanics Research Center Report EMRL 99-21, Dept. of Aerospace Engineering and Engineering Mechanics, University of Texas at Austin (2000).

[2] K. M. Liechti, S. Roy, A. G. Arzoumanidis, S. J. Park, & M. Wang. Long term durability of adhesively bonded joints: Final report. Engineering Mechanics Research Laboratory Report EMRL 00-12, The University of Texas at Austin (2000).
[3] G. L. Roderick, R. A. Everett, & J. H. Crews. Debond propagation in composite-reinforced metals. ASTM STP 569, American Society for Testing and Materials, 295–306 (1975).
[4] T. R. Brussat & S. T. Chiu. Fatigue crack growth of bondline cracks in structural bonded joints. *J. Engineering Materials and Technology*, **100**, 39–45 (1978).
[5] S. Mall, W. S. Johnson, & R. A. Everett (1984). Cyclic debonding of adhesively bonded composites. In *Adhesive joints: Their formation, characteristics and testing*, pp. 639–658, K. L. Mittal, Ed. (Plenum Press, New York).
[6] W. S. Johnson & S. Mall, Delamination and debonding of materials. ASTM STP 876, W. S. Johnson, Ed., 189–199 (1985).
[7] C. Lin & K. M. Liechti. Similarity concepts in the fatigue fracture of adhesively bonded joints. *J. Adhesion*, **21**, 1–24 (1987).
[8] P. G. Charalambides, J. Lund, A. G. Evans, & R. M. McMeeking. A test specimen for determining the fracture resistance of bimaterial interfaces. *J. Appl. Mech.,* **56**, 77–82 (1989).
[9] P. G. Charalambides, H. C. Cao, J. Lund, & A. G. Evans. Development of a test specimen for measuring the mixed mode fracture resistance of bimaterial interfaces. *Mech. of Materials*, **8**, 269–283 (1990).
[10] K. M. Conley, J. E. Ritter, & T. J. Lardner. Subcritical crack growth along epoxy/glass interfaces. *J. Mater. Res*., **7**, 2621–2629 (1992).
[11] S. Mostovoy & E. J. Ripling. Influence of water on stress corrosion cracking of epoxy bonds. *J. Appl. Polymer Sci*., **13**, 1083–1111 (1969).
[12] J. Cognard. Environmental attack on adhesive joints studied by cleavage fracture. *J. Adhesion*, **26**, 155–169 (1988).
[13] J. E. Ritter, T. J. Lardner, A. J. Stewart, & G. C. Prakash. Crack propagation in polymer adhesive/glass sandwich specimens. *J. Adhesion*, **49**, 97–112 (1995).
[14] J. E. Ritter, T. J. Lardner, W. Grayeski, G. C. Prakash, & J. Lawrence. Fatigue crack propagation at polymer adhesive interfaces. *J. Adhesion*, **63**, 265–284 (1997).
[15] J. E. Ritter, J. R. Fox, D. J. Hutko, & T. J. Lardner. Moisture-assisted crack growth at epoxy-glass interfaces. *J. Materials Science*, **33**, 1–8 (1998).
[16] J. W. Wylde & J. K. Spelt. Measurement of adhesive joint fracture properties as a function of environmental degradation. *Int. J. Adhesion and Adhesives*, **18**, 237–246 (1998).
[17] G. Fernlund & J. K. Spelt. Mixed-mode fracture characterization of adhesive joints. *Composites Science and Technology*, **50**, 441–449 (1994).
[18] M. Fernando, W. W. Harjoprayitno, & A. Kinloch. A fracture mechanics study on the influence of moisture on the fatigue behavior of adhesively bonded aluminumalloy joints. *Int. J. Adhesion and Adhesives*, **16**, 113–119 (1996).
[19] J. K. Jethwa & A. J. Kinloch. The fatigue and durability behavior of automotive adhesives: Part I. Fracture mechanics tests. *J. Adhesion*, **61**, 71–95 (1997).
[20] R. A. Dickie, L. P. Haack, J. K. Jethwa, A. J. Kinloch, & J. F. Watts. The fatigue and durability behavior of automotive adhesives: Part II. Failure mechanisms. *J. Adhesion*, **66**, 39–59 (1998).
[21] E. Sancaktar. Mixed-mode fatigue failure in structural adhesives. *Fatigue and Fracture Mechanics*, Vol. 29, ASTM STP 1332, T. L. Panontin and S. D. Sheppard, Eds., American Society for Testing and Materials, West Conshohocken, PA (1999).

[22] Z. Suo & J. W. Hutchinson. Sandwich test specimens for measuring interface crack toughness. *Mater. Sci. Engineering*, A**107**, 135–143 (1989).
[23] M. Dessureault & J. K. Spelt. Observations of fatigue crack initiation and propagation in an epoxy adhesive. *Int. J. Adhesion and Adhesives*, **17**, 183–195 (1997).
[24] H. Chai. A note on crack trajectory in an elastic strip bounded by rigid substrates. *Int. J. Fracture*, **32**, 211–213 (1987).